arXiv:2206.11089v3 [physics.atom-ph] 24 Jun 2022

Optically enhanced discharge excitation and trapping of ^{39}Ar

Y.-Q. Chu,[1] Z.-F. Wan,[1] F. Ritterbusch,[1,*] W.-K. Hu,[1] J.-Q. Gu,[1] S.-M. Hu,[1] Z.-H. Jia,[2,3] W. Jiang,[1] Z.-T. Lu,[1,†] L.-T. Sun,[2,4] A.-M. Tong,[1] J. S. Wang,[1] and G.-M. Yang[1]

[1] *University of Science and Technology of China, 96 Jinzhai Road, Hefei 230026, China*
[2] *Institute of Modern Physics, Chinese Academy of Sciences, Lanzhou 730000, China*
[3] *School of Nuclear Science and Technology, Lanzhou University, Lanzhou 730000, China*
[4] *School of Nuclear Science and Technology, University of Chinese Academy of Sciences, Beijing 100049, China*

We report on a two-fold increase of the ^{39}Ar loading rate in an atom trap by enhancing the generation of metastable atoms in a discharge source. Additional atoms in the metastable $1s_5$ level (Paschen notation) are obtained via optically pumping both the $1s_4 - 2p_6$ transition at 801 nm and the $1s_2 - 2p_6$ transition at 923 nm. By solving the master equation for the corresponding six-level system, we identify these two transitions to be the most suitable ones and encounter a transfer process between $1s_2$ and $1s_4$ when pumping both transitions simultaneously. We calculate the previously unknown frequency shifts of the two transitions in ^{39}Ar and confirm the results with trap loading measurements. The demonstrated increase in the loading rate enables a corresponding decrease in the required sample size, uncertainty and measurement time for ^{39}Ar dating, a significant improvement for applications such as dating of ocean water and alpine ice cores.

I. INTRODUCTION

The noble gas radioisotope ^{39}Ar with a half-life of 268 ± 8 years [1, 2] has long been identified as an ideal dating isotope for water and ice in the age range 50-1800 years due to its chemical inertness and uniform distribution in the atmosphere [3, 4]. However, its extremely low isotopic abundances of $10^{-17} - 10^{-15}$ in the environment have posed a major challenge in the analysis of ^{39}Ar. In the past, it could only be measured by Low-Level Counting, which requires several tons of water or ice [5].

In recent years, the sample size for ^{39}Ar dating has been drastically reduced by the emerging method Atom Trap Trace Analysis (ATTA), which detects individual atoms via their fluorescence in a magneto-optical trap (MOT). This laser-based technique was originally developed for ^{81}Kr and ^{85}Kr [6–9] and has later been adapted to ^{39}Ar, realizing dating of groundwater, ocean water and glacier ice [10–13]. The latest state-of-the-art system reaches an ^{39}Ar loading rate of ∼10 atoms/h for modern samples and an ^{39}Ar background of ∼0.1 atoms/h [14, 15]. Still, its use in applications like ocean circulation studies and dating of alpine glaciers is hampered by the low count rate, which determines the measurement time, precision and sample size.

Laser cooling and trapping of argon atoms in the ground level is not feasible due to the lack of suitable lasers at the required vacuum ultra violet (VUV) wavelength. As it is the case for all noble gas elements, argon atoms need to be excited to the metastable level $1s_5$ where the $1s_5 - 2p_9$ cycling transition at 811 nm can be employed for laser cooling and trapping (Paschen notation [16] is used here, the corresponding levels in Racah notation [17] can be found in Fig. 7 in Appendix A). The $1s_5$ level is ∼10 eV above the ground level and, in operational ATTA instruments, is populated by electron-impact excitation in a RF-driven discharge with an efficiency of only $10^{-4} - 10^{-3}$. Increasing this efficiency would raise the loading rate of ^{39}Ar accordingly.

Since the discharge excites atoms into not only the metastable $1s_5$ but also many other excited levels, the metastable $1s_5$ population can be enhanced by transferring atoms from these other excited levels to the metastable $1s_5$ via optical pumping (Fig. 1). This mechanism has been demonstrated in a spectroscopy cell for argon with an increase of 81% [18, 19] and for xenon with an increase by a factor of 11 [20, 21]. It has also been observed in an argon beam with an increase of 21% [18]. While these experiments were done on stable and abundant isotopes, a 60 % increase in loading rate has recently been observed for the rare isotopes ^{81}Kr and ^{85}Kr [22].

In this work, we theoretically and experimentally examine the enhancement of metastable production by optical pumping for the rare ^{39}Ar as well as the abundant argon isotopes. We identify the $1s_4 - 2p_6$ transition at 801 nm and the $1s_2 - 2p_6$ transition at 923 nm as the most suitable candidates. Implementing the enhancement scheme for ^{39}Ar on these transitions requires knowing the respective frequency shifts, which we calculate and experimentally confirm. Moreover, loading rate measurements support the theoretically predicted transfer process between $1s_2$ and $1s_4$ levels when driving the 923-nm and 801-nm transitions simultaneously.

A. Transfer efficiency

We solve the Lindblad master equation (see details in Appendix B) for the 6-level system shown in Fig. 1(a) which corresponds to the even argon isotopes without hyperfine structure. The resulting steady-state solution $\widetilde{\rho}_{55}(t \to +\infty)$ for the final population in the metastable

* florian@ustc.edu.cn
† ztlu@ustc.edu.cn

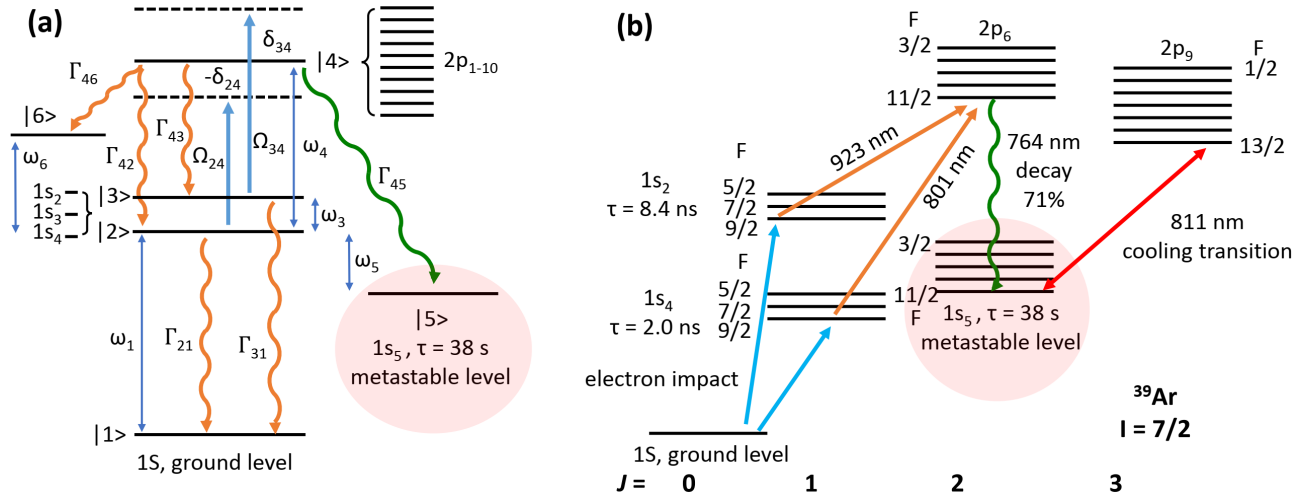


Figure 1: (a) Scheme for enhancing the population in the metastable level $1s_5$ by driving the $1s-2p$ levels with Rabi frequencies Ω_{24}, Ω_{34} and detunings δ_{24}, δ_{34}. Γ_{ij} denotes the spontaneous emission rate from level i to j. (b) The optical pumping scheme chosen in this work on the $1s_4-2p_6$ transition at 801 nm and $1s_2-2p_6$ transition at 923 nm, shown for ^{39}Ar which has a nuclear spin $I=7/2$.

level can be obtained analytically as a function of the initial populations in $|2\rangle$ and $|3\rangle$, using the initial condition

$$\widetilde{\rho}_{ij}(t=0)=0 \quad \text{for} \quad (i,j)\neq(2,2) \text{ and } (i,j)\neq(3,3). \quad (1)$$

If only one transition is driven, e.g. $\Omega_{34}=0$, then $\widetilde{\rho}_{55}(t\to+\infty)$ simplifies to the expressions given in [22]. We use these expressions to calculate the transfer efficiency $\widetilde{\rho}_{55}(t\to+\infty)$ for the different $1s-2p$ transitions in even argon isotopes as a function of laser power. The transitions with the highest transfer efficiencies are shown in Table I (see Table III in Appendix C for all transitions).

Table I: Argon transitions with the highest transfer efficiencies from each $1s$ level, calculated for a laser beam of 9-mm diameter and different powers P. For driving both transitions simultaneously (bottom row) an equal population in $1s_2$ and $1s_4$ and equal power P for each laser beam is assumed.

Lower level	Upper level	λ(nm)	$\widetilde{\rho}_{55}(t\to+\infty)$	
			$P=0.5$ W	$P\to+\infty$W
$1s_4$	$2p_6$	801	0.03	0.05
$1s_3$	$2p_{10}$	1047	0.77	0.77
$1s_2$	$2p_6$	923	0.15	0.17
$1s_2+1s_4$	$2p_6$	801+923	0.12	0.08

From the metastable level $1s_3$ (see Fig. 7 in Appendix C), the $1s_3-2p_{10}$ transition at 1047 nm has the highest transfer efficiency of 77 %. Since $1s_3$ is also metastable, only a few mW of laser power are needed to saturate the transition. However, experimentally we only achieve an increase in the metastable $1s_5$ population of ∼10 % by pumping this transition. Since the increase in the population of the metastable $1s_5$ is the product of the transfer efficiency (=0.77, Table I) and the initial population in the $1s_3$, it follows that the latter is only 10%/0.77 = 13% of that in the metastable $1s_5$. Given this limitation, optical pumping on $1s_3$ is not investigated further in this work.

The transfer efficiency from $1s_2$ is the highest for the 923-nm transition to $2p_6$, reaching a high-power limit of 17 %. From $1s_4$ the transfer efficiency is the highest for the 801-nm transition to $2p_6$, reaching a high-power limit of 5 %. Since the populations of these levels in the argon discharge are not known, the actual increase in the metastable population needs to be determined experimentally. In the following we focus on these two transitions as illustrated in Fig. 1(b) for the odd isotope ^{39}Ar.

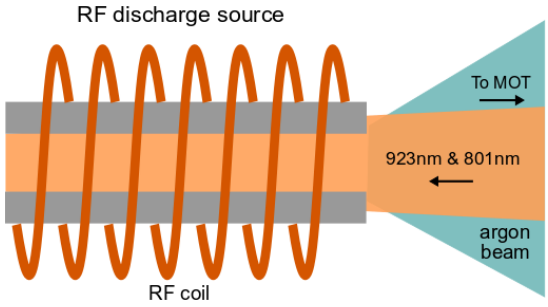


Figure 2: RF-driven discharge source of metastable argon atoms in the ATTA setup. The optical pumping laser beams are sent into the source counter-propagating to the atomic beam.

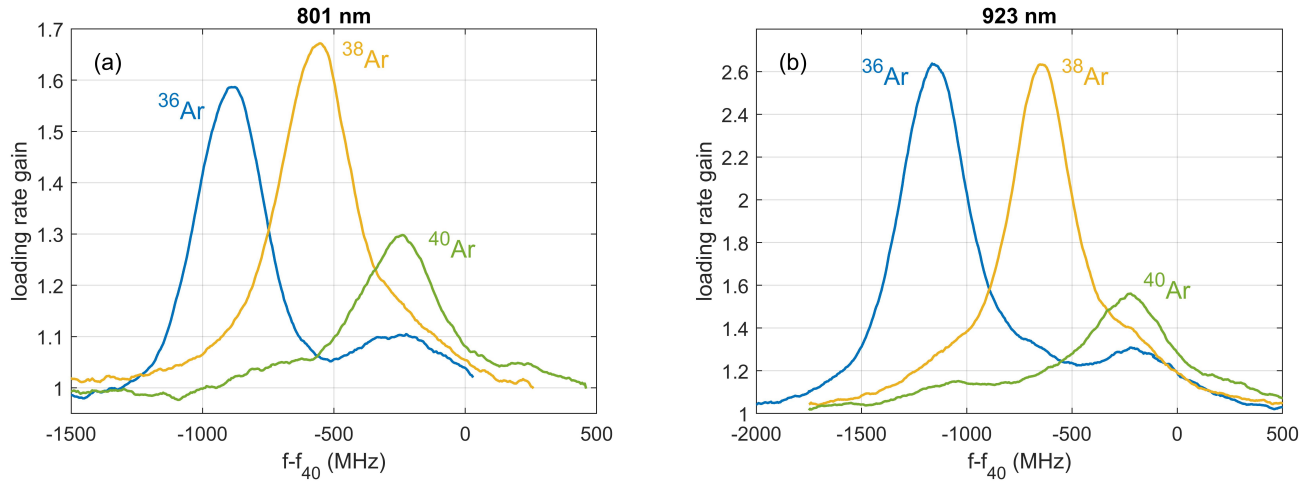


Figure 3: Gain in the MOT loading rate for the abundant argon isotopes vs frequency of the (a) 801-nm and (b) 923-nm optical pumping light, measured in the enriched sample. For each transition, f_{40} denotes the resonance frequency of ^{40}Ar at rest as monitored in a spectroscopy cell.

Interestingly, when these two transitions are driven simultaneously (i.e. $\Omega_{24} \neq 0, \Omega_{34} \neq 0$) the final population in the metastable level ρ_{55} is smaller than the sum of the individually driven transitions (see bottom row of table I). This effect is the consequence of stimulated emission from $2p_6$ to $1s_4$ by the 801-nm light, together with the 923-nm light effectively transferring atoms from $1s_2$ to $1s_4$. In the same way atoms are also transferred from $1s_4$ to $1s_2$. However, since the decay rate to the ground level from $1s_4$ is three times higher than from $1s_2$ (see Fig. 7 in Appendix A), the total increase in the metastable level is lower than the sum of the individually driven transitions. As the laser power increases also the stimulated emission increases, leading to a further decrease in the combined transfer efficiency to the metastable level.

B. Isotope shifts and hyperfine splittings for ^{39}Ar

The total frequency shifts of ^{39}Ar for the 801-nm and 923-nm transitions consist of the isotope shifts and the hyperfine splittings. The hyperfine coefficients of ^{39}Ar for $1s_2$ and $1s_4$ were measured in [23], whereas for $2p_6$ they can be calculated from the corresponding hyperfine coefficients measured for ^{37}Ar [24], using the measured nuclear magnetic dipole moments and electric quadrupole moments of ^{39}Ar and ^{37}Ar [22, 24–26]. The resulting hyperfine coefficients are shown in Table V in Appendix D. Isotope shifts of neither the 801-nm transition nor the 923-nm transition for any argon isotope have been found in the literature. The isotope shifts for ^{36}Ar and ^{38}Ar have therefore been measured in this work (see below), allowing us to calculate the isotope shifts for ^{39}Ar [22, 27, 28]. The resulting isotope shifts and hyperfine splittings for ^{39}Ar relative to ^{40}Ar are given in Table VI in Appendix D.

II. EXPERIMENTAL SETUP

For measuring the metastable population increase by optical pumping in ^{39}Ar as well as the stable argon isotopes, we use an ATTA system as described in [14]. Metastable argon atoms are generated in a RF-driven discharge by electron impact (Fig. 2) and are subsequently laser cooled and detected in a magneto-optical trap. Single ^{39}Ar atoms are detected via their 811-nm fluorescence in the MOT using an electron-multiplying charged coupled device (EMCCD) camera. During a measurement of ^{39}Ar (^{39}Ar/Ar=8×10^{-16} in modern air), the stable and abundant ^{38}Ar (^{38}Ar/Ar=0.06 % in air) is measured as well to account for drifts in the trap loading efficiency. The loading rate of ^{38}Ar for this normalization purpose is measured by depopulating the MOT with a quenching transition and detecting the emitted fluorescence [7, 14]. For testing optical pumping on ^{38}Ar and the other stable argon isotopes the loading rate is measured by first clearing the MOT with a quenching transition and then the initial linear part of the rising slope of the MOT fluorescence is measured [29].

For optical pumping, we shine in the 923 nm and 801 nm laser beams counter-propagating to the atomic beam (Fig. 2). The laser beams are weakly focused and slightly larger than the inner diameter of the source tube (⌀10 mm). The optical pumping light is generated by tapered amplifiers seeded with diode lasers, providing up to 1.0 W of usable laser power at 801 nm and 1.6 W at 923 nm. For measuring the different argon isotopes, the laser frequency needs to be tuned and stablilized over several GHz. For this purpose, the two lasers are

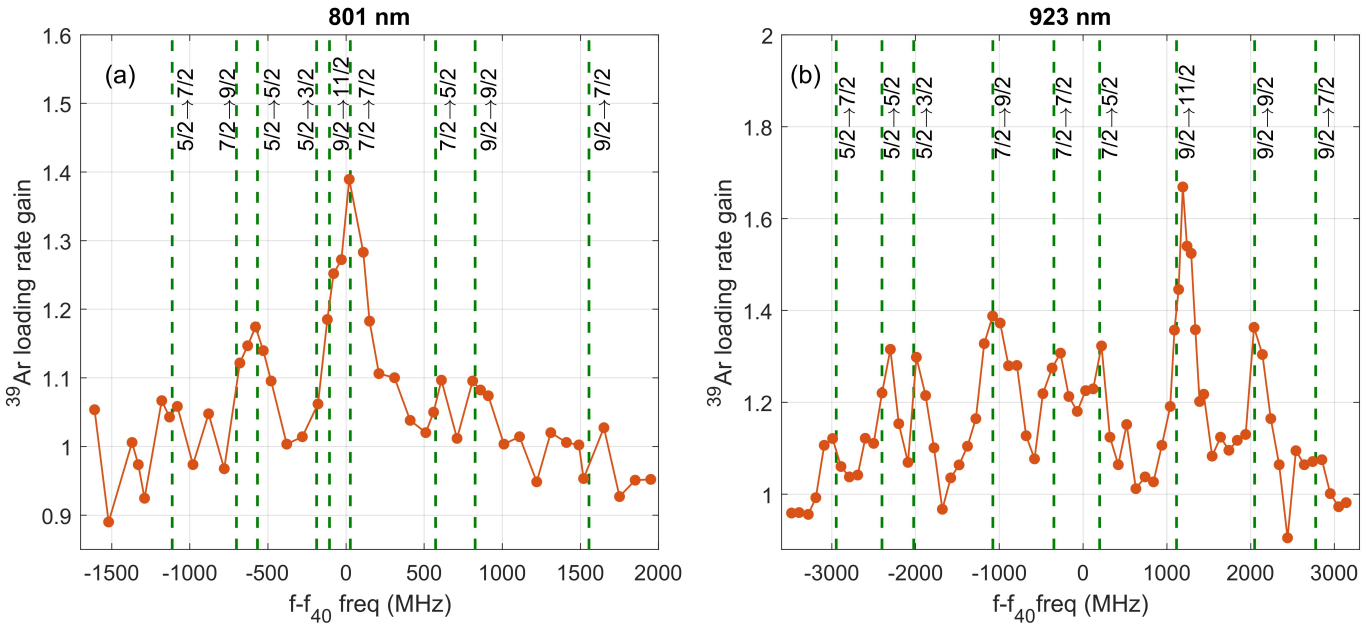


Figure 4: ^{39}Ar loading rate gain versus frequency of the (a) 801-nm and (b) 923-nm light, measured in the enriched sample. f_{40} denotes the resonance frequency of ^{40}Ar at rest as monitored in a spectroscopy cell. The Doppler-shift obtained for ^{40}Ar has been subtracted from the frequency to obtain the ^{39}Ar frequency spectrum at rest. The error of each ^{39}Ar data point is ∼5 %. The dashed green lines indicate the calculated frequencies of the hyperfine transitions.

locked by a scanning transfer cavity lock [30, 31], using a diode laser locked to the 811-nm cooling transition of metastable ^{40}Ar as the master. In order to increase counting statistics for ^{39}Ar, we use an enriched sample prepared by an electromagnetic mass separation system [32]. In the enriched sample, ^{40}Ar is largely and ^{36}Ar partially removed so that ^{39}Ar and ^{38}Ar are enriched by a factor ∼ 200. The ratio of ^{39}Ar and ^{38}Ar is not changed in the enrichment process [33], which is important for the normalization described above. The ^{40}Ar, ^{36}Ar and ^{38}Ar abundances in the enriched sample are 60 %, 30 % and 10 %, respectively.

III. RESULTS AND DISCUSSION

The loading rate of the stable argon isotopes is measured versus the frequencies of the 801-nm and 923-nm light (Fig. 3). A clear increase in the loading rate is observed for all isotopes. For ^{40}Ar we obtain most probable Doppler shifts around −230 MHz in agreement with the expected temperature of the liquid-nitrogen-cooled atomic beam. The small ^{40}Ar feature mirrored on the positive detuning side is likely caused by the optical pumping light reflected at the window behind the source. The window is partially coated by metal which has been sputtered by argon ions that are produced in the discharge. From the observed resonances for ^{36}Ar and ^{38}Ar we obtain the isotope shifts with respect to ^{40}Ar for the 801-nm as well as the 923-nm transition shown in Table IV. Based on these measured isotope shifts, we calculate the isotope shifts for ^{39}Ar (Table IV) using King plots [27]. Interestingly, the loading rate of ^{36}Ar shows a pronounced increase also at the ^{40}Ar resonance for both, the 801-nm and the 923-nm transition. Looking closely, an increase in loading rate is visible for each isotope at the resonances of the other two isotopes. This additional increase is likely caused by metastable exchange collisions, e.g. transferring an increase in the metastable population of ^{40}Ar to that of ^{36}Ar. The maximum loading rate gain is lower for ^{40}Ar than for the less abundant ^{36}Ar and ^{38}Ar. This difference is discussed in more detail below.

Fig. 4 shows the ^{39}Ar loading rate gain vs frequency of the 801-nm and 923-nm light. For both transitions, a clear increase in the loading rate is observed. For 923 nm, the $F = 9/2 \rightarrow 11/2$ transition is the strongest as expected from the multiplicity and transition strength [34]. Moreover, the measurements confirm the other calculated hyperfine transitions. For 801 nm, the overlap of the $F = 9/2 \rightarrow 11/2$ and $F = 7/2 \rightarrow 7/2$ transition is the strongest. The loading rate increase is lower compared to that achieved with the 923-nm light. Accordingly, the different hyperfine transitions are resolved less clearly. Nevertheless, the measurements are in good agreement with the calculated hyperfine transitions. In order to address not only one but two hyperfine levels of

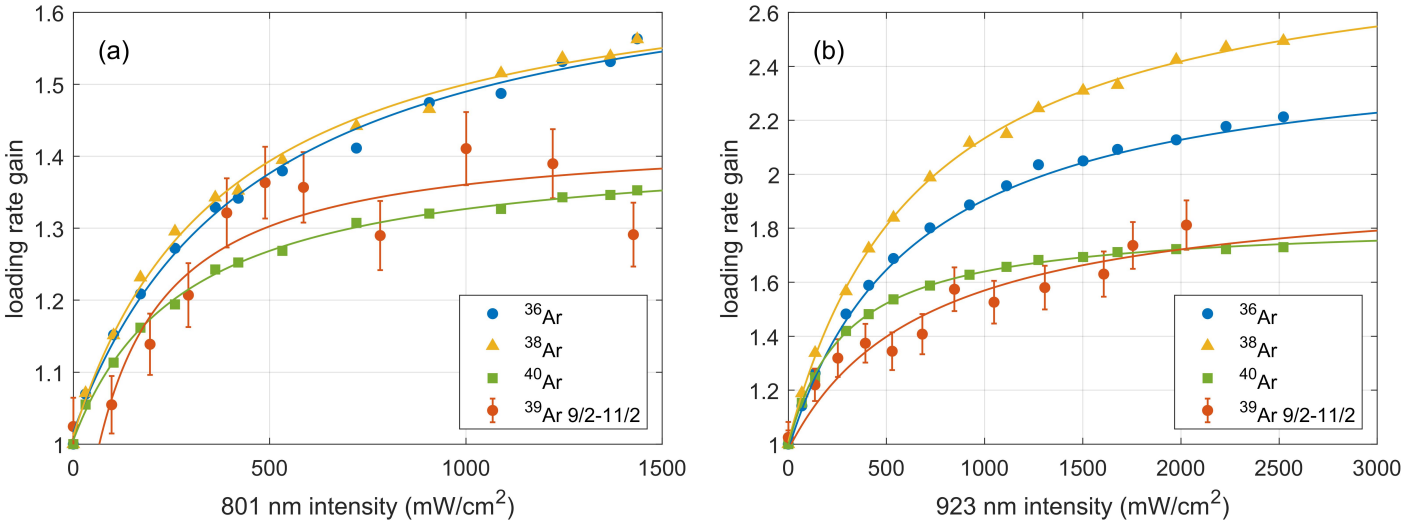


Figure 5: (a) Loading rate gain of the argon isotopes vs laser power of the (a) 801-nm light and (b) 923-nm light, measured with the enriched argon sample. The lines are saturation fits according to the expressions given in [22].

^{39}Ar, we add sidebands to the 801-nm and 923-nm light. At 801 nm no increase is detectable by adding a sideband resonant with the overlap of the $F = 7/2 \rightarrow 9/2$ and $F = 5/2 \rightarrow 5/2$ transitions. At 923 nm we observe a maximum increase of only ∼10 %, although according to Fig. 4(b) an increase of 40 % appears possible. Likely, the increase by adding a sideband is compensated by the decrease due to the lower laser power on the carrier frequency.

The loading rate gain as a function of laser power is shown in Fig. 5. As already observed in Fig. 3(a), the maximum loading rate gain is lower for ^{40}Ar than for the less abundant ^{36}Ar and ^{38}Ar. This may be caused by the higher density of ^{40}Ar leading to a stronger trapping of the 764 nm fluorescence (see Fig. 1), which can quench other metastable atoms. Moreover, the saturation intensity is significantly lower for ^{40}Ar than for ^{36}Ar and ^{38}Ar. This may also be caused by the higher density of ^{40}Ar, leading to trapping of the re-emitted 801-nm and 923-nm light. The saturation intensity for ^{39}Ar is difficult to assess due to the large measurement uncertainties and the contribution from neighbouring hyperfine levels.

Table II lists the maximum loading rate gains of the different argon isotopes for the 801-nm and the 923-nm transitions, as well as for both transitions driven together. As predicted by the calculation in section I A and Appendix B, driving both transitions simultaneously results in a lower gain than the addition of the individual gains. This result confirms the transfer due to stimulated emission between $1s_2$ and $1s_4$ via the intermediate $2p_6$, driven by the 923-nm and 801-nm light. For ^{39}Ar a two-fold gain in the loading rate is obtained by optical pumping when simultaneously using 801-nm and 923-nm light and addressing the $F = 9/2$ level. According to the loading rate gain obtained for the other hyperfine levels (Fig. 4), if sidebands are introduced with additional laser power a near three-fold gain in the loading rate should be possible.

Table II: Loading rate gains obtained for different argon isotopes and different transitions, measured in the enriched argon sample.

Isotope	801 nm	923 nm	801 nm + 923 nm
^{40}Ar	1.4	1.7	1.8
^{38}Ar	1.6	2.5	2.8
^{36}Ar	1.6	2.2	2.6
^{39}Ar	1.4	1.8	2.0

As mentioned above and observed in Fig. 5, the loading rate gain varies for different isotopes. Moreover, we observe that the loading rate gain depends on density and sample composition. In order to examine the dependence, we measure the ^{36}Ar and ^{40}Ar loading rate gains vs. argon pressure in the chamber at the outlet of the source tube (Fig. 6). In this measurement, atmospheric argon (abundances of ^{40}Ar, ^{36}Ar and ^{38}Ar are 99.6 %, 0.33 % and 0.06 %, respectively) is used instead of the enriched sample. The loading rate gains of the two isotopes differ significantly. For ^{36}Ar the loading rate gain increases with the argon pressure whereas for ^{40}Ar the loading rate gain decreases beyond a maximum. Moreover, the loading rate gain for ^{36}Ar in this measurement with atmospheric argon reaches the value 3.3 whereas it is only 2.2 when measured with the enriched sample (^{36}Ar abundance=30 %) as in Fig. 5. These findings indicate that the populations of the $1s$-levels in the dis-

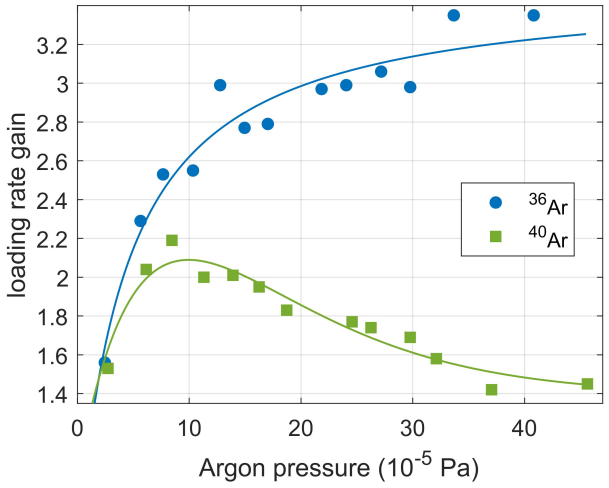


Figure 6: Loading rate gain vs argon pressure in the chamber at the outlet of the source tube (Fig. 2) for the 923-nm transition, measured with atmospheric argon. The pressure inside the source tube is considerably higher than at the outlet of the source tube. The lines are guides-to-the-eye.

charge depend on pressure and composition. These dependences might be caused by various mechanisms such as trapping of light from the VUV ground level transitions, which together with the optical pumping light can produce metastable argon atoms.

IV. CONCLUSION AND OUTLOOK

We have realized a two-fold increase of the ^{39}Ar loading rate in an atom trap system via optical pumping in the discharge source. A three-fold increase is expected by adding sidebands with additional laser power that cover all the hyperfine levels of ^{39}Ar. Similarly, we obtain an increase of the MOT loading rate by a factor 2-3 for the stable argon isotopes ^{36}Ar, ^{38}Ar and ^{40}Ar. We observe that the loading rate gain varies for different isotopes and that it depends on the argon pressure in the discharge as well as the abundance of the respective isotope. We assign these dependences to the complex population dynamics of the 1s-levels in the discharge via mechanisms such as radiation trapping and metastable exchange collisions. Consequently, using the method presented here for practical ^{39}Ar analysis requires a stable control of the pressure so that the loading rate gain due to optical pumping for both ^{39}Ar and ^{38}Ar stays constant during measurements.

The hitherto unknown isotope shifts in ^{36}Ar and ^{38}Ar as well as the ^{39}Ar spectra for the 801-nm and 923-nm transitions have been measured in this work. They constitute an important contribution to the efforts on optically generating metastable argon via resonant two-photon excitation [35, 36]. For a more precise measurement of the hyperfine coefficients and the isotope shifts, spectroscopy on samples highly enriched in ^{39}Ar will be necessary [37, 38].

The presented method for enhanced production of metastable argon can be directly implemented in existing ATTA setups to increase the ^{39}Ar loading rate by a factor 2-3. For state-of-the-art ATTA systems, the ^{39}Ar loading rate is ∼10 atoms/h. For ^{39}Ar analysis at a precision level of 5 %, this loading rate leads to a measuring time of ∼50 h during which the ^{39}Ar background in the ATTA system increases linearly with time. Therefore, the two-fold increase in ^{39}Ar loading rate realized in this work constitutes a significant advance for measuring time, precision and sample size of ^{39}Ar analysis in environmental applications such as dating of alpine ice cores and large scale ocean surveys.

ACKNOWLEDGMENTS

This work is funded by the National Natural Science Foundation of China (41727901, 41961144027, 41861224007), National Key Research and Development Program of China (2016YFA0302200), Anhui Initiative in Quantum Information Technologies (AHY110000).

Y.-Q. Chu and Z.-F. Wan contributed equally to this work.

An edited version of this paper was published by APS Physical Review A 105, 063108 (2022). *Copyright 2022 American Physical Society.*

Appendix A: Argon $1s - 2p$ transitions

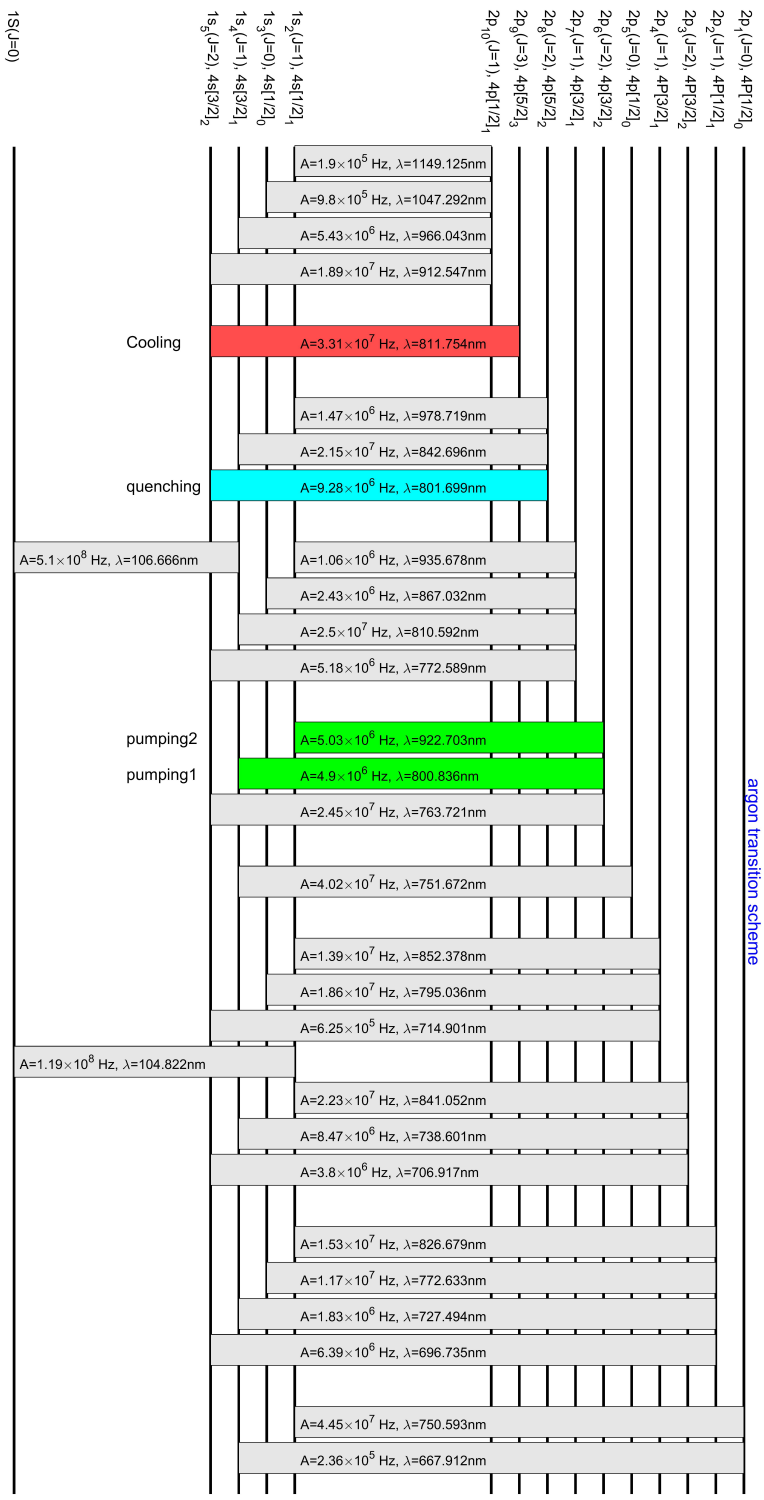


Figure 7: Argon transition scheme calculated based on [39] and adopted from [40, 41]. Levels with capital letter in the Racah notation refer to $j_{\text{core}} = 1/2$ while levels with small letters refer to $j_{\text{core}} = 3/2$.

Appendix B: Master equation

The 6-level system for optical pumping of the even argon isotopes without hyperfine structures is illustrated in Fig. 1. As described in section I A, $|1\rangle$ is the ground level and $|5\rangle$ the metastable level for laser cooling and trapping. Atoms in levels $|2\rangle$ and $|3\rangle$ can be transferred to $|5\rangle$ by driving the transition to $|4\rangle$ followed by spontaneous decay. $|6\rangle$ represents other levels that atoms can decay to from $|4\rangle$. Choosing the energy of level $|2\rangle$ as zero, $-\hbar\omega_1, \hbar\omega_3, \hbar\omega_4, -\hbar\omega_5$ and $\hbar\omega_6$ are the energies of the corresponding levels relative to $|2\rangle$. In the interaction picture, the Hamiltonian of this atomic system interacting with the laser field is

$$\hat{H} = \hat{H}_A + \hat{H}_{AF}, \tag{B1}$$

where

$$\begin{aligned}\hat{H}_A = \hbar\omega_4|4\rangle\langle 4| - \hbar\omega_1|1\rangle\langle 1| + \hbar\omega_3|3\rangle\langle 3| \\ - \hbar\omega_5|5\rangle\langle 5| + \hbar\omega_6|6\rangle\langle 6|\end{aligned} \tag{B2}$$

is the atomic Hamiltonian and

$$\begin{aligned}\hat{H}_{AF} = \quad & \frac{\hbar}{2}(\Omega_{24}^* \sigma_{24} e^{i\omega_{24}t} + \Omega_{24}\sigma_{42}e^{-i\omega_{24}t}) \\ & + \frac{\hbar}{2}(\Omega_{34}^*\sigma_{34}e^{i\omega_{34}t} + \Omega_{34}\sigma_{43}e^{-i\omega_{34}t})\end{aligned} \tag{B3}$$

is the Hamiltonian that describes the interaction of the atoms with the light field. Here, ω_{24} and ω_{34} are the laser frequencies of the incident light, Ω_{24} and Ω_{34} are the corresponding Rabi frequencies and $\sigma_{ij} = |i\rangle\langle j|$ are the spin operators. With the unitary transformation $U = \exp(i\omega_{24}t|4\rangle\langle 4| + i(\omega_{24} - \omega_{34})t|3\rangle\langle 3|)$, the quantum level $|\psi\rangle$ changes to

$$\widetilde{|\psi\rangle} = U|\psi\rangle. \tag{B4}$$

In this Schrödinger picture, the Hamiltonian becomes

$$\begin{aligned}\widetilde{H} &= UHU^\dagger + i\hbar(\partial_t U)U^\dagger \\ &= -\hbar\delta_{24}\sigma_{44} - \hbar\omega_1\sigma_{11} - \hbar\omega_5\sigma_{55} + \hbar\omega_6\sigma_{66} \\ &+ \hbar(\delta_{34} - \delta_{24})\sigma_{33} + \frac{\hbar}{2}(\Omega_{24}\sigma_{42} + \Omega_{34}\sigma_{43} + h.c.)\end{aligned} \tag{B5}$$

where $\delta_{24} = \omega_{24} - \omega_4$ and $\delta_{34} = \omega_{34} - (\omega_4 - \omega_3)$ are the detunings of the light with respect to the transition frequencies.

The Lindblad master equation for the system including the spontaneous emission can be written as

$$\begin{aligned}\frac{d\widetilde{\rho}}{dt} &= \frac{1}{i\hbar}[\widetilde{H}, \widetilde{\rho}] \\ &+ \Gamma_{42}(\sigma_{24}\widetilde{\rho}\sigma_{42} - \frac{1}{2}\widetilde{\rho}\sigma_{44} - \frac{1}{2}\sigma_{44}\widetilde{\rho}) \\ &+ \Gamma_{21}(\sigma_{12}\widetilde{\rho}\sigma_{21} - \frac{1}{2}\widetilde{\rho}\sigma_{22} - \frac{1}{2}\sigma_{22}\widetilde{\rho}) \\ &+ \Gamma_{45}(\sigma_{54}\widetilde{\rho}\sigma_{45} - \frac{1}{2}\widetilde{\rho}\sigma_{44} - \frac{1}{2}\sigma_{44}\widetilde{\rho}) \\ &+ \Gamma_{46}(\sigma_{64}\widetilde{\rho}\sigma_{46} - \frac{1}{2}\widetilde{\rho}\sigma_{44} - \frac{1}{2}\sigma_{44}\widetilde{\rho}) \\ &+ \Gamma_{43}(\sigma_{34}\widetilde{\rho}\sigma_{43} - \frac{1}{2}\widetilde{\rho}\sigma_{44} - \frac{1}{2}\sigma_{44}\widetilde{\rho}) \\ &+ \Gamma_{31}(\sigma_{13}\widetilde{\rho}\sigma_{31} - \frac{1}{2}\widetilde{\rho}\sigma_{33} - \frac{1}{2}\sigma_{33}\widetilde{\rho})\end{aligned} \tag{B6}$$

where Γ_{ij} is the spontaneous emission rate from $|i\rangle$ to $|j\rangle$. These equations describe the time evolution of $\widetilde{\rho}_{ij} = \langle i|\widetilde{\rho}|j\rangle$ and can be simplified to

$$\begin{aligned}\frac{d\widetilde{\rho}_{11}}{dt} &= \Gamma_{21}\widetilde{\rho}_{22} + \Gamma_{31}\widetilde{\rho}_{33} \\ \frac{d\widetilde{\rho}_{22}}{dt} &= \Gamma_{42}\widetilde{\rho}_{44} - \Gamma_{21}\widetilde{\rho}_{22} + \frac{i}{2}(\Omega_{24}\widetilde{\rho}_{24} - \Omega_{24}^*\widetilde{\rho}_{42}) \\ \frac{d\widetilde{\rho}_{44}}{dt} &= -(\Gamma_{42} + \Gamma_{45} + \Gamma_{46} + \Gamma_{43})\widetilde{\rho}_{44} \\ &+ \frac{i}{2}(\Omega_{24}^*\widetilde{\rho}_{42} - \Omega_{24}\widetilde{\rho}_{24}) + \frac{i}{2}(\Omega_{34}^*\widetilde{\rho}_{43} - \Omega_{34}\widetilde{\rho}_{34}) \\ \frac{d\widetilde{\rho}_{55}}{dt} &= \Gamma_{45}\widetilde{\rho}_{44} \\ \frac{d\widetilde{\rho}_{66}}{dt} &= \Gamma_{46}\widetilde{\rho}_{44} \\ \frac{d\widetilde{\rho}_{33}}{dt} &= \Gamma_{43}\widetilde{\rho}_{44} - \Gamma_{31}\widetilde{\rho}_{33} + \frac{i}{2}(\Omega_{34}\widetilde{\rho}_{34} - \Omega_{34}^*\widetilde{\rho}_{43}) \\ \frac{d\widetilde{\rho}_{42}}{dt} &= -\frac{1}{2}(\Gamma_{42} + \Gamma_{21} + \Gamma_{45} + \Gamma_{46} + \Gamma_{43} - 2i\delta_{24})\widetilde{\rho}_{42} \\ &+ \frac{i\Omega_{24}}{2}(\widetilde{\rho}_{44} - \widetilde{\rho}_{22}) - \frac{i\Omega_{34}}{2}\widetilde{\rho}_{32} \\ \frac{d\widetilde{\rho}_{43}}{dt} &= -\frac{1}{2}(\Gamma_{42} + \Gamma_{31} + \Gamma_{45} + \Gamma_{46} + \Gamma_{43} - 2i\delta_{34})\widetilde{\rho}_{43} \\ &+ \frac{i\Omega_{34}}{2}(\widetilde{\rho}_{44} - \widetilde{\rho}_{33}) - \frac{i\Omega_{24}}{2}\widetilde{\rho}_{23} \\ \frac{d\widetilde{\rho}_{32}}{dt} &= -\frac{1}{2}(\Gamma_{21} + \Gamma_{31} + 2i(\delta_{34} - \delta_{24}))\widetilde{\rho}_{32} \\ &- \frac{i\Omega_{34}^*}{2}\widetilde{\rho}_{42} + \frac{i\Omega_{24}}{2}\widetilde{\rho}_{34}\end{aligned} \tag{B7}$$

Using that the population is initially in $|2\rangle$ and $|3\rangle$, i.e.

$$\begin{aligned}&\widetilde{\rho}_{22}(t=0) \neq 0\ ,\ \widetilde{\rho}_{33}(t=0) \neq 0 \\ &\widetilde{\rho}_{ij}(t=0) = 0,\ (i,j) \neq (2,2), (i,j) \neq (3,3),\end{aligned} \tag{B8}$$

then for the steady-state

$$\frac{d\widetilde{\rho}}{dt}(t \to +\infty) = 0 \tag{B9}$$

Eq. B7 can be solved analytically using a computer algebra system, yielding the transfer efficiency $\widetilde{\rho}_{55}(t \to +\infty)$.

Appendix C: TRANSFER EFFICIENCIES FOR $1s$–$2p$ TRANSITIONS IN ^{40}Ar

To determine the most suitable transitions for optical pumping to the metastable level $1s_5$, we have theoretically investigated all the $1s-2p$ transitions in argon. The transfer efficiency for each transition has been calculated according to the derivation in Sec. I A and the results are compiled in Table III. For each $1s$ level we can thereby identify the transition with the highest transfer efficiency. Among these, we experimentally find the $1s_2-2p_6$ transition at 923 nm and the $1s_4-2p_6$ transition at 801 nm to be the strongest ones for optical pumping and therefore have chosen them for this work. A scheme of all $1s-2p$ transitions in argon is illustrated in Fig. 7 with the levels in Racah as well as in Paschen notation.

Table III: Transfer efficiencies $\widetilde{\rho}_{55}(t\to+\infty)$ for $1s-2p$ transitions in ^{40}Ar calculated for a laser beam with 9-mm diameter and different powers P. The transitions highlighted in bold are the ones with the highest transfer efficiency. The levels are provided in Paschen as well as in Racah notation.

Lower level	Upper level	λ (nm)	Transfer efficiency $\widetilde{\rho}_{55}(t\to+\infty)$	
			$P=0.5\,\mathrm{W}$	$P\to+\infty\mathrm{W}$
$1s_4$, $4s[3/2]_1$	$2p_{10}$, $4p[1/2]_1$	966.04	0.03	0.04
	$2p_8$, $4p[5/2]_2$	842.70	0.02	0.02
	$2p_7$, $4p[3/2]_1$	810.60	0.01	0.01
	$2p_6$, $4p[3/2]_2$	**800.84**	**0.03**	**0.05**
	$2p_4$, $4P[3/2]_1$	747.12	0.00	0.00
	$2p_3$, $4P[3/2]_2$	738.60	0.00	0.01
	$2p_2$, $4P[1/2]_1$	727.50	0.00	0.01
$1s_3$, $4s[1/2]_0$	**$2p_{10}$, $4p[1/2]_1$**	**1047.30**	**0.77**	**0.77**
	$2p_7$, $4p[3/2]_1$	867.03	0.17	0.17
	$2p_4$, $4P[3/2]_1$	795.04	0.04	0.04
	$2p_3$, $4P[1/2]_1$	772.63	0.27	0.27
$1s_2$, $4s[1/2]_1$	$2p_{10}$, $4p[1/2]_1$	1149.13	0.05	0.13
	$2p_8$, $4p[5/2]_2$	978.72	0.05	0.06
	$2p_7$, $4p[3/2]_1$	935.68	0.02	0.03
	$2p_6$, $4p[3/2]_2$	**922.70**	**0.15**	**0.17**
	$2p_4$, $4P[3/2]_1$	852.38	0.00	0.00
	$2p_3$, $4P[3/2]_2$	841.05	0.03	0.03
	$2p_2$, $4P[1/2]_1$	826.68	0.04	0.05

Appendix D: ISOTOPE, HYPERFINE, AND TOTAL FREQUENCY SHIFTS FOR THE 801-nm AND 923-nm TRANSITION IN ^{39}Ar

Realizing optical pumping for the odd argon isotopes requires knowledge of the frequency shifts for the employed 801-nm and 923-nm transition. The total frequency shift is the sum of the isotope shift and the hyperfine shift. The isotope shifts for ^{39}Ar have not been measured and were calculated based on the measured isotope shifts for the stable isotopes (see Sec. I B). The resulting isotope shifts for ^{36}Ar, ^{38}Ar and ^{39}Ar are shown in Table IV. The hyperfine constants of the involved levels have been measured for ^{39}Ar or can be calculated from measurements for ^{37}Ar (see Sec. I B). The resulting hyperfine shifts for the different hyperfine levels are compiled in Table VI together with the isotope shifts and the total frequency shifts.

Table IV: Isotope shifts relative to ^{40}Ar for the 801-nm and 923-nm transitions.

Transition nm	Isotope	Isotope shift MHz
801	^{36}Ar	$-640(10)^{a}$
	^{38}Ar	$-290(10)^{a}$
	^{39}Ar	$-128(16)^{b}$
923	^{36}Ar	$-960(10)^{a}$
	^{38}Ar	$-445(10)^{a}$
	^{39}Ar	$-202(16)^{b}$

[a] Measured in this work.
[b] Calculated in this work.

Table V: Hyperfine coefficients A and B for ^{39}Ar and different levels.

Wavelength nm	level	A MHz	B MHz
801	$1s_4$	$-334(2)^{a}$	$-24(3)^{a}$
	$2p_6$	$-163(31)^{b}$	$-63(11)^{b}$
923	$1s_2$	$-712(1)^{a}$	$84(6)^{a}$
	$2p_6$	$-163(31)^{b}$	$-63(11)^{b}$

[a] Reference [23].
[b] Reference [24].

Table VI: Isotope, hyperfine and total frequency shifts for the 801-nm and 923-nm transitions in ^{39}Ar. The hyperfine shift is relative to the center of gravity of the fine-structure term and the isotope shift is relative to ^{40}Ar.

Transition nm	Isotope shift MHz	Lower level $1s_4/1s_2$	Upper level $2p_6$	HFS shift MHz	Total shift MHz
801	−128(16)	$F = 5/2$	$F = 3/2$	-61(275)	-189(275)
			$F = 5/2$	-440(198)	−567(199)
			$F = 7/2$	−985(92)	−1113(93)
		$F = 7/2$	$F = 5/2$	701(198)	573 (199)
			$F = 7/2$	155(92)	27(93)
			$F = 9/2$	−574(46)	−702(49)
		$F = 9/2$	$F = 7/2$	1682(92)	1555(93)
			$F = 9/2$	953(46)	826(49)
			$F = 11/2$	21(214)	−106(214)
923	−202(16)	$F = 5/2$	$F = 3/2$	-1820(275)	-2022(275)
			$F = 5/2$	−2198(198)	−2401(199)
			$F = 7/2$	−2744(92)	−2946(93)
		$F = 7/2$	$F = 5/2$	400(198)	197(199)
			$F = 7/2$	-146(92)	-348(93)
			$F = 9/2$	−875(46)	−1077(49)
		$F = 9/2$	$F = 7/2$	2978(92)	2776(93)
			$F = 9/2$	2249(46)	2047(49)
			$F = 11/2$	1317(214)	1115(214)

[1] R. W. Stoenner, O. A. Schaeffer, and S. Katcoff, Science **148**, 1325 (1965).
[2] J. Chen, Nuclear Data Sheets **149**, 1 (2018).
[3] D. Lal, Earth Science and Meteorites **7**, 115 (1963).
[4] H. H. Loosli and H. Oeschger, Earth and Planetary Science Letters **5**, 191 (1968).
[5] H. Loosli, Earth and Planetary Science Letters **63**, 51 (1983).
[6] C. Y. Chen, Y. M. Li, K. Bailey, T. P. O'Connor, L. Young, and Z.-T. Lu, Science **286**, 1139 (1999).
[7] W. Jiang, K. Bailey, Z.-T. Lu, P. Mueller, T. O'Connor, C.-F. Cheng, S.-M. Hu, R. Purtschert, N. Sturchio, Y. Sun, W. Williams, and G.-M. Yang, Geochimica et Cosmochimica Acta **91**, 1 (2012).
[8] Z.-T. Lu, P. Schlosser, W. M. Smethie, N. C. Sturchio, T. P. Fischer, B. M. Kennedy, R. Purtschert, J. P. Severinghaus, D. K. Solomon, T. Tanhua, and R. Yokochi, Earth-Science Reviews **138**, 196 (2014).
[9] L. Tian, F. Ritterbusch, J.-Q. Gu, S.-M. Hu, W. Jiang, Z.-T. Lu, D. Wang, and G.-M. Yang, Geophysical Research Letters **46**, 6636 (2019).
[10] W. Jiang, W. Williams, K. Bailey, A. M. Davis, S.-M. Hu, Z.-T. Lu, T. P. O'Connor, R. Purtschert, N. C. Sturchio, Y. R. Sun, and P. Mueller, Phys. Rev. Lett. **106**, 103001 (2011).
[11] F. Ritterbusch, S. Ebser, J. Welte, T. Reichel, A. Kersting, R. Purtschert, W. Aeschbach-Hertig, and M. K. Oberthaler, Geophysical Research Letters **41**, 6758 (2014).
[12] S. Ebser, A. Kersting, T. Stöven, Z. Feng, L. Ringena, M. Schmidt, T. Tanhua, W. Aeschbach, and M. Oberthaler, Nature Communications **9** (2018).
[13] Z. Feng, P. Bohleber, S. Ebser, L. Ringena, M. Schmidt, A. Kersting, P. Hopkins, H. Hoffmann, A. Fischer, W. Aeschbach, and M. K. Oberthaler, Proceedings of the National Academy of Sciences **116**, 8781 (2019).
[14] A. L. Tong, J.-Q. Gu, G.-M. Yang, S.-M. Hu, W. Jiang, Z.-T. Lu, and F. Ritterbusch, Review of Scientific Instruments **92**, 063204 (2021).
[15] J.-Q. Gu, A. L. Tong, G.-M. Yang, S.-M. Hu, W. Jiang, Z.-T. Lu, R. Purtschert, and F. Ritterbusch, Chemical Geology **583**, 120480 (2021).
[16] F. Paschen, Annalen der Physik **365**, 405 (1919).
[17] G. Racah, Physical Review **61**, 537 (1942).
[18] M. Hans, Bachelor thesis, Heidelberg University (2014).
[19] A. Frölian, Bachelor thesis, Heidelberg University (2015).
[20] G. T. Hickman, J. D. Franson, and T. B. Pittman, Optics Letters **41**, 4372 (2016).

[21] H. P. Lamsal, J. D. Franson, and T. B. Pittman, Optics Express **28**, 24079 (2020).

[22] Z.-Y. Zhang, F. Ritterbusch, W.-K. Hu, X.-Z. Dong, C. Y. Gao, W. Jiang, S.-Y. Liu, Z.-T. Lu, J. S. Wang, and G.-M. Yang, Phys. Rev. A **101**, 053429 (2020).

[23] W. Traub, F. L. Roesler, M. M. Robertson, and V. W. Cohen, J. Opt. Soc. Am. **57**, 1452 (1967).

[24] A. Klein, B. Brown, U. Georg, M. Keim, P. Lievens, R. Neugart, M. Neuroth, R. Silverans, L. Vermeeren, and ISOLDE Collaboration, Nuclear Physics A **607**, 1 (1996).

[25] L. Armstrong, *Theory of the Hyperfine Structure of Free Atoms* (Wiley-Interscience, New York, 1971) oCLC: 639161041.

[26] N. J. Stone, Journal of Physical and Chemical Reference Data **44**, 031215 (2015).

[27] W. H. King, J. Opt. Soc. Am. **53**, 638 (1963).

[28] K. Heilig and A. Steudel, Atomic Data and Nuclear Data Tables Nuclear Charge and Moment Distributions, **14**, 613 (1974).

[29] C. F. Cheng, G. M. Yang, W. Jiang, Y. R. Sun, L. Y. Tu, and S. M. Hu, Optics Letters **38**, 31 (2013).

[30] W. Z. Zhao, J. E. Simsarian, L. A. Orozco, and G. D. Sprouse, Review of Scientific Instruments **69**, 3737 (1998).

[31] S. Subhankar, A. Restelli, Y. Wang, S. L. Rolston, and J. V. Porto, Review of Scientific Instruments **90**, 043115 (2019).

[32] Z. Jia, A. Tong, L. Sun, Y. Liu, J. Liu, Q. Wu, X. Fang, W. Yang, Y. Guo, F. Ritterbusch, Z.-T. Lu, W. Jiang, G. Yang, and Q. Chen, Review of Scientific Instruments **91**, 033309 (2020).

[33] A. L. Tong, J.-Q. Gu, Z.-H. Jia, G.-M. Yang, S.-M. Hu, W. Jiang, Z.-T. Lu, F. Ritterbusch, and L.-T. Sun, Review of Scientific Instruments **93**, 023203 (2022).

[34] O. Axner, J. Gustafsson, N. Omenetto, and J. D. Winefordner, Spectrochimica Acta Part B: Atomic Spectroscopy **59**, 1 (2004).

[35] J. S. Wang, F. Ritterbusch, X.-Z. Dong, C. Gao, H. Li, W. Jiang, S.-Y. Liu, Z.-T. Lu, W.-H. Wang, G.-M. Yang, Y.-S. Zhang, and Z.-Y. Zhang, Phys. Rev. Lett. **127**, 023201 (2021).

[36] X.-Z. Dong, F. Ritterbusch, D.-F. Yuan, J.-W. Yan, W.-T. Chen, W. Jiang, Z.-T. Lu, J. S. Wang, X.-A. Wang, and G.-M. Yang, Phys. Rev. A **105**, L031101 (2022).

[37] J. Welte, I. Steinke, M. Henrich, F. Ritterbusch, M. K. Oberthaler, W. Aeschbach-Hertig, W. H. Schwarz, and M. Trieloff, Review of Scientific Instruments **80**, 113109 (2009).

[38] W. Williams, Z.-T. Lu, K. Rudinger, C.-Y. Xu, R. Yokochi, and P. Mueller, Phys. Rev. A **83**, 012512 (2011).

[39] A. Kramida, Yu. Ralchenko, J. Reader, and NIST ASD Team, NIST Atomic Spectra Database (version 5.7.1), [Online]. Available: `https://physics.nist.gov/asd` [Apr 14 2020]. National Institute of Standards and Technology, Gaithersburg, MD. DOI: https://doi.org/10.18434/T4W30F (2019).

[40] F. Ritterbusch, diploma thesis, Heidelberg University (2009).

[41] J. Welte, PhD thesis, Heidelberg University (2011).